






## Article

# Atmospheric Pressure Solvothermal Synthesis of Nanoscale SnO<sub>2</sub> and Its Application in Microextrusion Printing of a Thick-Film Chemosensor Material for Effective Ethanol Detection

Nikita A. Fisenko <sup>1,2</sup> , Ivan A. Solomatov <sup>3</sup>, Nikolay P. Simonenko <sup>1,\*</sup>, Artem S. Mokrushin <sup>1</sup> , Philipp Yu. Gorobtsov <sup>1</sup> , Tatiana L. Simonenko <sup>1</sup> , Ivan A. Volkov <sup>4</sup> , Elizaveta P. Simonenko <sup>1,\*</sup>  and Nikolay T. Kuznetsov <sup>1</sup>

- <sup>1</sup> Kurnakov Institute of General and Inorganic Chemistry of the Russian Academy of Sciences, 31 Leninsky pr., Moscow 119991, Russia
- <sup>2</sup> Higher Chemical College of the Russian Academy of Sciences, D. Mendeleev University of Chemical Technology of Russia, 9 Miusskaya sq., Moscow 125047, Russia
- <sup>3</sup> Basic Department of Inorganic Chemistry and Materials Science, National Research University “Higher School of Economics”, 20 Myasnitskaya str., Moscow 101978, Russia
- <sup>4</sup> Moscow Institute of Physics and Technology, National Research University, 9 Institutskiy per., Dolgoprudny 141701, Russia
- \* Correspondence: n\_simonenko@mail.ru (N.P.S.); ep\_simonenko@mail.ru (E.P.S.)



**Citation:** Fisenko, N.A.; Solomatov, I.A.; Simonenko, N.P.; Mokrushin, A.S.; Gorobtsov, P.Y.; Simonenko, T.L.; Volkov, I.A.; Simonenko, E.P.; Kuznetsov, N.T. Atmospheric Pressure Solvothermal Synthesis of Nanoscale SnO<sub>2</sub> and Its Application in Microextrusion Printing of a Thick-Film Chemosensor Material for Effective Ethanol Detection. *Sensors* **2022**, *22*, 9800. <https://doi.org/10.3390/s22249800>

Academic Editor: Dimitris Tsoukalas

Received: 3 November 2022

Accepted: 12 December 2022

Published: 14 December 2022

**Publisher’s Note:** MDPI stays neutral with regard to jurisdictional claims in published maps and institutional affiliations.



**Copyright:** © 2022 by the authors. Licensee MDPI, Basel, Switzerland. This article is an open access article distributed under the terms and conditions of the Creative Commons Attribution (CC BY) license (<https://creativecommons.org/licenses/by/4.0/>).

**Abstract:** The atmospheric pressure solvothermal (APS) synthesis of nanocrystalline SnO<sub>2</sub> (average size of coherent scattering regions (CSR)—7.5 ± 0.6 nm) using tin acetylacetonate as a precursor was studied. The resulting nanopowder was used as a functional ink component in microextrusion printing of a tin dioxide thick film on the surface of a Pt/Al<sub>2</sub>O<sub>3</sub>/Pt chip. Synchronous thermal analysis shows that the resulting semiproduct is transformed completely into tin dioxide nanopowder at 400 °C within 1 h. The SnO<sub>2</sub> powder and the resulting film were shown to have a cassiterite-type structure according to X-ray diffraction analysis, and IR spectroscopy was used to establish the set of functional groups in the material composition. The microstructural features of the tin dioxide powder were analyzed using scanning (SEM) and transmission (TEM) electron microscopy: the average size of the oxide powder particles was 8.2 ± 0.7 nm. Various atomic force microscopy (AFM) techniques were employed to investigate the topography of the oxide film and to build maps of surface capacitance and potential distribution. The temperature dependence of the electrical conductivity of the printed SnO<sub>2</sub> film was studied using impedance spectroscopy. The chemosensory properties of the formed material when detecting H<sub>2</sub>, CO, NH<sub>3</sub>, C<sub>6</sub>H<sub>6</sub>, C<sub>3</sub>H<sub>6</sub>O and C<sub>2</sub>H<sub>5</sub>OH, including at varying humidity, were also examined. It was demonstrated that the obtained SnO<sub>2</sub> film has an increased sensitivity (the sensory response value was 1.4–63.5) and selectivity for detection of 4–100 ppm C<sub>2</sub>H<sub>5</sub>OH at an operating temperature of 200 °C.

**Keywords:** tin oxide; thick film; atmospheric pressure solvothermal synthesis; microextrusion printing; gas sensor; electrical conductivity; nanopowder; ink; ethanol; humidity

## 1. Introduction

Tin dioxide has been attracting scientific attention all over the world for decades, both as an individual material [1–4] and as a component of more complex substances, especially transparent electrodes, including ITO [5,6], SnGaO [7], ZnSnO (ZTO) [8,9], SnO<sub>2</sub>:F (FTO) [10], Al-Sn-Zn-O (ATZO) [11], SnO<sub>2</sub>@N [12] and others. This material is a wide-bandgap semiconductor ( $E_g \sim 3.6$  eV [1,3,13]) of n-type with a resistance of  $(1\text{--}3) \cdot 10^{-3} \Omega \cdot \text{cm}$  [14] and optical transmission in the visible light of 85% at 50–450 nm film thickness [1,14]. Among the functional characteristics, the gas sensitivity of tin dioxide is

particularly prominent, and the spectrum of analyte gases is quite wide, including triethylamine (TEA,  $\text{N}(\text{CH}_2\text{CH}_3)_3$ ) [15], formaldehyde ( $\text{HCHO}$ ), trichlorofluoromethane ( $\text{CCl}_3\text{F}$ ), methane ( $\text{CH}_4$ ), hydrogen sulfide ( $\text{H}_2\text{S}$ ) [16], benzene ( $\text{C}_6\text{H}_6$ ), toluene ( $\text{C}_7\text{H}_8$ ), ethanol ( $\text{C}_2\text{H}_6\text{O}$ ) [15,17–20], heptafluorobutyronitrile ( $\text{C}_4\text{F}_7\text{N}$ ) [21], nitrogen dioxide ( $\text{NO}_2$ ) [22,23], acetone ( $(\text{CH}_3)_2\text{CO}$ ), isopropyl alcohol (IPA,  $\text{C}_3\text{H}_8\text{O}$ ) [18], hydrogen ( $\text{H}_2$ ) [24], water vapor ( $\text{H}_2\text{O}$ ), carbon monoxide ( $\text{CO}$ ) [25] and chloroform ( $\text{CHCl}_3$ ) [26]. Due to this fact,  $\text{SnO}_2$  is often used as the main component of chemoresistive gas sensors. It is also known that the microstructural and functional properties of metal oxides largely depend on the synthesis method used (sol-gel technology, chemical precipitation, glycol-citrate synthesis, hydro- or solvothermal method, gas-phase synthesis techniques, etc.). At the same time, the solvothermal method, due to the combination of simplicity and variability depending on the synthesis conditions, allows the formation of nanoscale tin dioxide with a particle size of 2–13 nm [22,24]. “Classically, this method is carried out in sealed reactors under elevated temperatures and pressures, which sometimes leads to technical complications and limitations, which can be avoided by using atmospheric pressure solvothermal (APS) synthesis” [27].

When manufacturing various devices, it is often necessary to form  $\text{SnO}_2$ -based films. As a rule, such classical methods as dip-coating [28,29], spin-coating [30,31], physical vapor deposition (PVD) [32] and chemical vapor deposition (CVD) [26,33] are used for this purpose. These methods have some disadvantages, including limitations on the accuracy of dosing and targeting upon deposition of the material on the substrate surface, the risk of a gradient across the film thickness, high energy costs and precursor consumption, poor reproducibility, etc. Additive technologies, which enable the automated manufacturing of both bulk and planar materials, are attracting a considerable amount of attention today [34–37]. In this case, the reproducibility and targeting accuracy of the material application, as well as the speed of the process, increase significantly. One of the most promising and understudied methods of forming thick-film semiconductor materials, including chemosensory ones, is microextrusion printing [38–45], which is currently more frequently used for biomedical applications, in particular for printing organs and bones [46,47].

Thus, the purpose of this work was to study the atmospheric pressure solvothermal synthesis of nanoscale tin dioxide and its application in the formation of the corresponding thick film via microextrusion printing, as well as to study the microstructure and the electrophysical and chemosensitive properties of the obtained material. Particularly, it was necessary to evaluate the effectiveness of tin acetylacetonate as a precursor for the synthesis of tin dioxide with a developed surface that provides high chemosensory characteristics for the resulting oxide film.

## 2. Materials and Methods

### 2.1. Materials

A solution of tin acetylacetonate (0.2 mol/L) in acetylacetone ( $\text{C}_5\text{H}_8\text{O}_2$ , 98%, Chimmed, Moscow, Russia), ethanol ( $\text{C}_2\text{H}_5\text{OH}$ , 96%, Chimmed, Moscow, Russia) and distilled water was used in this work without further purification. In order to measure chemosensory properties of the obtained  $\text{SnO}_2$  thick film, synthetic air (Zero Air Calibration Gas, oxygen volume fraction  $20.9 \pm 0.5\%$ ) was used, as well as calibration gas mixtures containing the following gases: 1%  $\text{H}_2$  ( $\pm 0.015\%$ ), 200 ppm  $\text{CO}$ , 200 ppm  $\text{NH}_3$ , 200 ppm  $\text{C}_6\text{H}_6$ , 200 ppm  $\text{C}_3\text{H}_6\text{O}$  ( $\pm 5$  ppm) and 200 ppm  $\text{C}_2\text{H}_5\text{OH}$  in air.

### 2.2. APS Synthesis of Nanosized $\text{SnO}_2$

Tin dioxide nanopowder was obtained by APS method. In a typical experiment, a 6.5 mL solution of tin acetylacetonate in acetylacetone was added dropwise to a 120 mL mixture of ethanol and distilled water ( $\text{C}_2\text{H}_5\text{OH}$  volume fraction—30%) in a glass beaker under stirring, resulting in the formation of microemulsion and initiation of complex hydrolysis accompanied by the precipitation of solid phase particles. In order to intensify this process, the reaction system under stirring was heated up to 90 °C and kept at this

temperature for 1 h. Separation of the precipitate from the mother liquor was carried out by stepwise centrifugation, after which the substance was washed twice with ethyl alcohol (dispersion was carried out using an ultrasonic bath) to remove acetylacetone formed as a by-product. Then, the precipitate was dried at 100 °C for 2 h in a drying oven in convection mode. At the next stage, the thermal behavior of the formed powder was studied using synchronous thermal analysis, and the conditions of additional heat treatment (400 °C, 1 h) required for complete decomposition of the semiproduct and formation of nanocrystalline SnO<sub>2</sub> powder were determined.

### 2.3. Microextrusion Printing of SnO<sub>2</sub> Thick Film

The obtained tin dioxide nanopowder was further used to prepare a functional ink, which was a paste with a viscosity of about 0.5 Pa·s, in order to form a thick oxide film by microextrusion printing. For this purpose, the SnO<sub>2</sub> powder was homogenized in  $\alpha$ -terpineol in the presence of ethyl cellulose. Printing of the film on the surface of a specialized Pt/Al<sub>2</sub>O<sub>3</sub>/Pt-chip was performed using a three-coordinate positioning system and a pneumatic dispenser (system pressure 3.5 atm) equipped with a dosing device as well as G27-gauge needle (inner diameter 210  $\mu$ m). The chip was an aluminum oxide substrate (Ra = 100 nm, geometric dimensions 4.1  $\times$  25.5  $\times$  0.6 mm) with platinum interdigitated electrodes (platinum layer thickness about 20  $\mu$ m) on one side and a platinum meander microheater on the reverse side (Figure 1). The movement speed of the dispenser over the substrate surface was 0.5 mm/s, the pulse duration for paste dispensing was 0.8 s and the pulse interval was 0.5 s. The lateral dimensions of the formed oxide film were 5  $\times$  3 mm. After printing, the film was dried at 40 °C for 24 h followed by a heat treatment at 400 °C (1 h) to remove residual solvent and to decompose the organic components. The thickness of the oxide layer corresponded to the thickness of the platinum interdigitated electrodes and was 20  $\mu$ m.

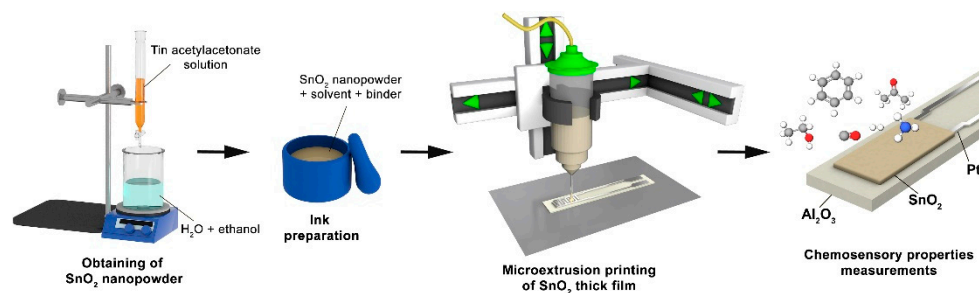


Figure 1. Scheme of SnO<sub>2</sub> thick film formation.

### 2.4. Instrumentation

IR transmission spectra of powders as suspensions in vaseline oil placed between KBr glasses were recorded using an InfraLUM FT-08 FT-IR spectrometer (Lumex, Saint Petersburg, Russia) in the wavenumber range of 350–4000 cm<sup>−1</sup>.

The thermal behavior of the semiproduct was analyzed using a combined DSC/DTA/TGA analyzer SDT-Q600 (TA Instruments, New Castle, DE, USA) in Al<sub>2</sub>O<sub>3</sub> crucibles in an air flow (250 mL/min) at a heating rate of 10 °/min in two modes (1—in the temperature range 25–1000 °C, sample mass 23 mg; 2—in the range 25–400 °C with holding at 400 °C for 1 h, sample mass 84 mg).

X-ray diffraction patterns of the semiproduct, SnO<sub>2</sub> powder, and oxide film were recorded on a D8 Advance X-ray diffractometer (Bruker, Bremen, Germany, CuK $\alpha$  = 1.5418 Å, Ni-filter, E = 40 keV, I = 40 mA, integration time = 0.3 s/point, step = 0.02°) in the 2 $\theta$  range of 10–80°.

The microstructure of the obtained SnO<sub>2</sub> powder and the printed film was studied using a three-beam NVision 40 workstation (Carl Zeiss, Oberkochen, Germany) and a Solver Pro-M scanning probe microscope (NT-MDT, Zelenograd, Russia) using ETALON HA-HR probes with a W<sub>2</sub>C conductive coating (resonance frequency ~230 kHz, rounding

radius <35 nm) in the modes of semicontact AFM, Kelvin-probe force microscopy (KPFM) and scanning capacitance microscopy (SCM).

The specific electrical conductivity of the SnO<sub>2</sub> film was studied by impedance spectroscopy using a professional electrochemical workstation based on a P-45X potentiostat/galvanostat with an impedance measurement unit FRA-24M (Electrochemical Instruments, Chernogolovka, Russia). Impedance measurements were carried out in air in the temperature range of 50–350 °C in the frequency interval of 1 MHz–0.4 Hz. The temperature of the sample was maintained by applying a voltage (QJ 3003H power supply; Ningbo JiuYuan Electronic, Ningbo, China) to the platinum microheater on the back side of the chip, and was controlled by a thermal imager Testo 868 (Testo, Lenzkirch, Germany). The electrical resistance of the material was calculated using ZView Scribner Associates, Inc. (Southern Pines, NC, USA) software (Version3.3c).

The chemoresistive responses were obtained using a special laboratory setup, a detailed description of which can be found in our earlier papers [43,48]. To measure the signal at different humidity levels, a specialized setup with a barboter was used, and the humidity of the gas mixture was monitored using a digital flow-through hygrometer “Eksis IVTM-7 K” (Eksis, Zelenograd, Russia). The responses to hydrogen (H<sub>2</sub>), carbon monoxide (CO), ammonia (NH<sub>3</sub>), benzene (C<sub>6</sub>H<sub>6</sub>), ethanol (C<sub>2</sub>H<sub>5</sub>OH) and acetone (C<sub>3</sub>H<sub>6</sub>O) were measured using the appropriate calibration gas mixtures with air.

The response was calculated using the following ratio:

$$S = R_{\text{air}}/R_g, \quad (1)$$

where  $R_g$  is the response at a given analytical gas concentration and  $R_{\text{air}}$  is the baseline response (synthetic air).

### 3. Results and Discussion

#### 3.1. Thermal Behavior of the Semiproduct

After drying at 100 °C, the thermal behavior of the obtained semiproduct was studied (Figure 2). In the first step, the analysis was carried out in a wide temperature range (25–1000 °C) (Figure 2a). As can be seen from the corresponding thermograms, when heating up to 250 °C, the mass loss of the powder is about 2.3%, which refers to the evaporation of residual solvents and sorbed atmospheric gases. Upon heating from 250 to 450 °C, the main stage of weight loss (11.7%), accompanied by two overlapping exothermic effects (with maxima at 301 and 342 °C) and related to oxidation of organic components contained in the powder, is observed. Further heating leads to slower mass loss ( $\Delta m$  is about 1.85% in the range 450–1000 °C). Thus, the total mass loss in the temperature range under consideration reached 15.83%, and the main processes occurred before 450 °C.

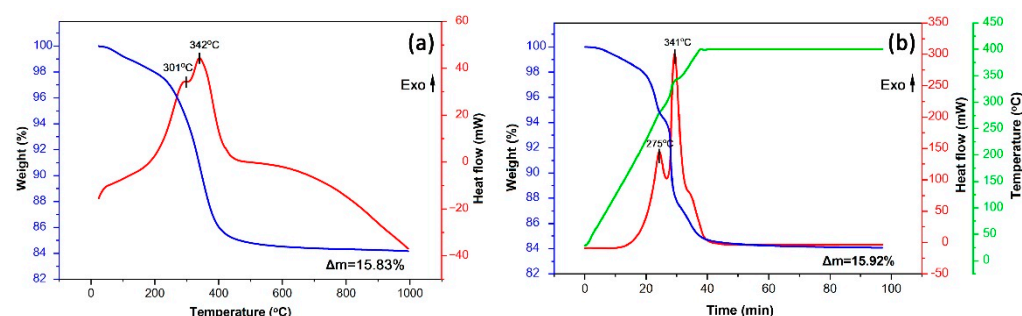


**Figure 2.** Thermal analysis results (weight—blue curve; heat flow—red curve; temperature—green curve) for the semiproduct in the temperature range of 25–1000 °C (a) and in the range of 25–400 °C with exposure to 400 °C for 1 h (b).

Next, in order to provide additional insights into the kinetics of the thermal transformation of the semiproduct, the dried powder was heated to 400 °C and exposed to that

temperature for 1 h (Figure 2b). Powder mass was also increased to 84 mg (up from 23 mg) for this experiment in order to achieve more detailed thermograms. As can be seen, the steps of mass loss and the corresponding thermal effects became more distinct. Thus, in this case in the 250–400 °C interval, not two but three stages of mass loss accompanied by energy release are already observed. The maxima of the first two of these thermal effects, compared with the preliminary thermal analysis in a wider temperature range, shifts to the low-temperature region (down to 275 and 341 °C, respectively). In the 350–400 °C interval, an additional shoulder on the DSC curve is observed, along with a mass loss of about 3%. Thus, oxidation of the organic components contained in the semiproduct is a multistep process. During further exposure at 400 °C for 1 h, a significant slowdown of the powder mass loss is observed ( $\Delta m = 0.89\%$ ). As a result, it was determined that the value of the final mass loss (15.92%) in this regime of semiproduct heat treatment even exceeds the value that was recorded when heating to 1000 °C, i.e., the kinetics of the oxidation process plays a more important role than temperature increase. Using the results of synchronous thermal analysis, the mildest mode of heat treatment (400 °C, 1 h) was determined, which allows achieving the complete transformation of the semiproduct and provides preservation of a high dispersion state for the formed tin dioxide powder.

### 3.2. Crystal Structure, Spectral Properties and Microstructure of the Semiproduct and SnO<sub>2</sub> Nanopowder

The crystalline structure of the semiproduct and the powder obtained as a result of additional heat treatment at 400 °C for one hour was studied by X-ray diffraction analysis (Figure 3a). Analysis of the corresponding diffractograms showed that the semiproduct is characterized by the crystal lattice of cassiterite (sp.gr  $P4_2/mnm$ , JCPDS No. 41-1445), typical for tin dioxide. At the same time, no crystalline impurities were found in its composition.

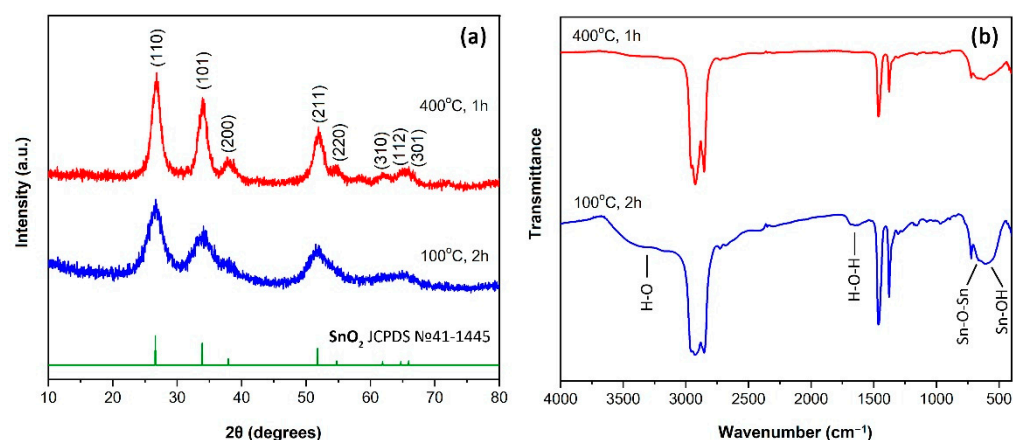


**Figure 3.** XRD patterns (a) and infrared spectra (b) of the semiproduct and SnO<sub>2</sub> nanopowder obtained by additional heat treatment.

As a result of additional heat treatment of the semiproduct, the crystal structure was preserved, but a decrease in the width and increase in the intensity of the reflexes can be observed, which indicates an increase in the average CRS size of X-rays. The average size of the CSR as well as the crystal lattice parameters for the powders under study were determined using full-profile analysis of the corresponding XRD patterns according to the Rietveld refinement method. Thus, for the semiproduct, the average size of the CSR was  $4.1 \pm 0.5$  nm, and the parameters of the crystal lattice have the following values:  $a = b = 4.73$  Å,  $c = 3.19$  Å. Additional heat treatment at 400 °C for one hour led to an increase in the average size of the CSR to  $7.5 \pm 0.6$  nm, as well as to some decrease in the crystal lattice parameters:  $a = b = 4.72$  Å,  $c = 3.18$  Å. In this case as well, no crystal impurities were revealed.



The set of functional groups in the obtained powders was studied by infrared spectroscopy (Figure 3b). Thus, unlike the SnO<sub>2</sub> nanopowder obtained after additional heat treatment, the spectrum of the semiproduct shows absorption band in the range of 1550–1750 cm<sup>−1</sup>, as well as a broad absorption band in the region of 3000–3700 cm<sup>−1</sup>, which relate to the vibrations of OH-groups in the material composition. The presence of hydroxyl groups in this case is also confirmed by the presence of a band at about 600 cm<sup>−1</sup> referring to the vibrations of the Sn-OH bond. In the case of both powders, in the wavenumber range of 450–800 cm<sup>−1</sup> there is an absorption band characteristic of SnO<sub>2</sub>, relating to the vibrations of Sn-O-Sn bonds, which is in agreement with the results of XRD analysis. It should be noted that the IR spectroscopy results also indicate the absence of any impurities in the studied powders. The absorption bands observed in the spectra with maxima at 2900, 1400, 1300 and 750 cm<sup>−1</sup> correspond to vibrations of functional groups of vaseline oil [49].

The microstructure of the obtained SnO<sub>2</sub> powder was studied by scanning (Figure 4a,b) and transmission electron microscopy (Figure 4c,d). As can be seen from the micrographs, the powder is characterized by a homogeneous microstructure, consisting of nanosized particles that are organized into globular agglomerates up to several tens of micrometers in size. According to SEM data, the average size of SnO<sub>2</sub> particles is 21 ± 2 nm. In this case, no impurity formations differing in shape and size were detected in the composition of the powder. The TEM results made it possible to specify the size and shape of the oxide nanoparticles. Thus, it was determined that their shape was close to spherical, and their average size had a value of 8.2 ± 0.7 nm, which was comparable to the average CSR size determined by XRD analysis. Thus, it was found that the SnO<sub>2</sub> powder obtained by the APS method is nanosized, has a homogeneous microstructure and does not contain any impurities.

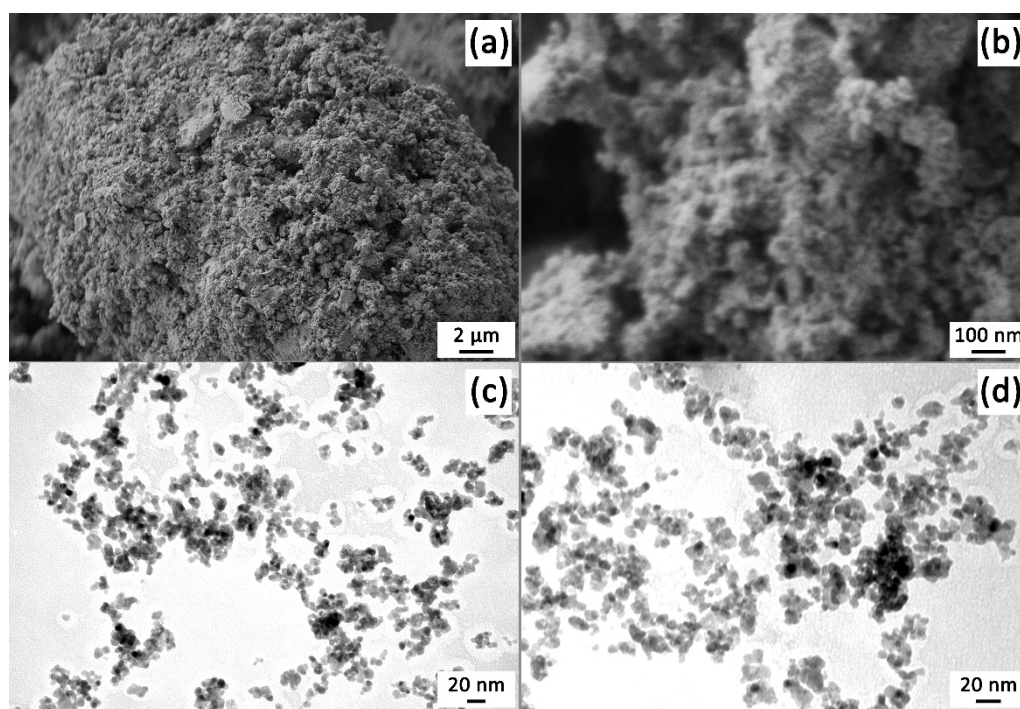


**Figure 4.** Microstructure of the obtained SnO<sub>2</sub> nanopowder: ((a,b) SEM; (c,d) TEM).

### 3.3. Crystal Structure and Microstructure of Thick SnO<sub>2</sub> Film

The crystal structure of the tin dioxide thick film printed on the surface of a specialized Pt/Al<sub>2</sub>O<sub>3</sub>/Pt chip was studied by XRD analysis. As can be seen from the diffractogram (Figure 5, left), the main signals, which are intense narrow reflexes, refer to the substrate components (polycrystalline α-Al<sub>2</sub>O<sub>3</sub> and platinum).

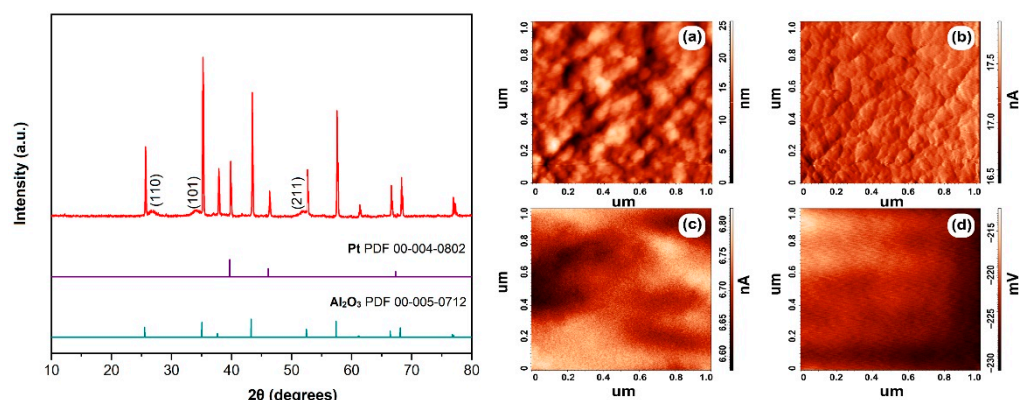


**Figure 5.** XRD pattern of the SnO<sub>2</sub> film on the surface of a specialized Pt/Al<sub>2</sub>O<sub>3</sub>/Pt chip (**left**), as well as AFM results (**right**)—topography (**a**) and amplitude mismatch mode during topography imaging (**b**), capacity distribution map (**c**) and surface potential distribution (**d**).

However, low-intensity reflexes of the applied SnO<sub>2</sub> film are clearly visible in their background. At the same time, it was shown that after the oxide film had been printed on the substrate surface, the crystal lattice characteristic of tin(IV) oxide with a cassiterite tetragonal structure (sp.gr.  $P4_2/mnm$ ) was preserved. The analysis of the X-ray diffraction made it possible to estimate the average CSR size for the formed oxide film, which was  $8.4 \pm 0.7$  nm. That is slightly higher compared to the nanopowder used for the preparation of functional inks. Nevertheless, the determined value of the average CSR size indicates that the material remains highly dispersed and that a nanocrystalline SnO<sub>2</sub> film is obtained, while the slight increase in crystallite size can be explained by an additional heat treatment of the microextrusion-printed layer in order to remove the solvent and binder.

The microstructure as well as some local electrophysical properties of the formed tin dioxide film were studied by atomic force microscopy (Figure 5a–d). From the above scanning results (both topography and mismatch amplitude), it is seen that the film consists of round-shaped agglomerates with a diameter of about 50 nm, which are composed of smaller particles. For a scanning area of 100 μm<sup>2</sup>, the arithmetic average roughness was 166 nm and the mean square roughness was 212 nm. For a scan area of up to 1 μm<sup>2</sup>, the mean square roughness is 3.7 nm and the maximum height difference does not exceed 25 nm, indicating that the material is relatively even. From the SCM and KPFM results, it is clear that the distribution of electrophysical characteristics, such as charge carrier and surface potential distribution, is highly uniform. The value of the electronic work function of the SnO<sub>2</sub> thick film under study was determined from the KPFM data, amounting to 5.048 eV, which is on the higher end of the values usually reported in the literature (4.7–5.2 eV [50–52]), which can be explained by the nanoscale state of the material or the conditions of coating heat treatment. According to published data, when tin dioxide nanoparticles are calcined, the energy of the conduction and valence band edges decrease, and the electronic work function value, therefore, increases [53].

The microstructure of the SnO<sub>2</sub> film surface was also studied using SEM (Figure 6). As can be seen from the micrographs, the oxide film is porous (both nanopores and pores up to 5 μm in size are observed), characterized by a regular microstructure without defects in the form of cracks, fractures or delaminations. The presence of uniformly distributed oxide microspheres of 2–5 μm in size, which are formed at the first stage of APS synthesis due to the formation of microemulsion, can be seen in the structure of the material. Analysis of the images obtained at high magnification allowed us to determine the average particle size, which was  $22 \pm 2$  nm. Thus, the application of the oxide film and its additional heat treatment had almost no effect on the size of the oxide particles of which it consists.

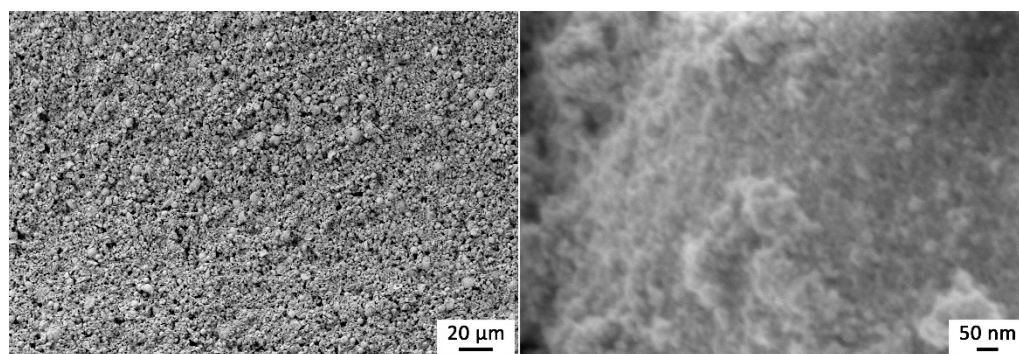


**Figure 6.** Microstructure of the printed SnO<sub>2</sub> thick film.

### 3.4. Electrical Conductivity of the Printed Oxide Film

At the next stage the electrophysical properties of the SnO<sub>2</sub> nanocrystalline film printed on the Pt/Al<sub>2</sub>O<sub>3</sub>/Pt chip surface were studied. Thus, using the impedance spectroscopy, frequency dependences of the complex impedance of the material in the temperature range of 50–350 °C within the frequency range of 1 MHz–0.4 Hz were obtained. Figure 7a shows an example of a typical hodograph obtained for the studied coating at a temperature of 100 °C. It can be seen that the hodograph has the form of a semicircle, slightly elongated along the abscissa axis, and can be described by an equivalent circuit including a resistance R (charge transfer resistance) and a constant phase element (CPE) connected in parallel. The series resistance (R<sub>s</sub>) is the resistance provided by the wires and contacts that complete the circuit. A similar type of hodograph has also been observed previously in the literature for tin dioxide-based films [54]. The overall electrical conductivity of the samples was determined using resistance R values calculated from impedance spectra obtained in the temperature range of 50–350 °C.

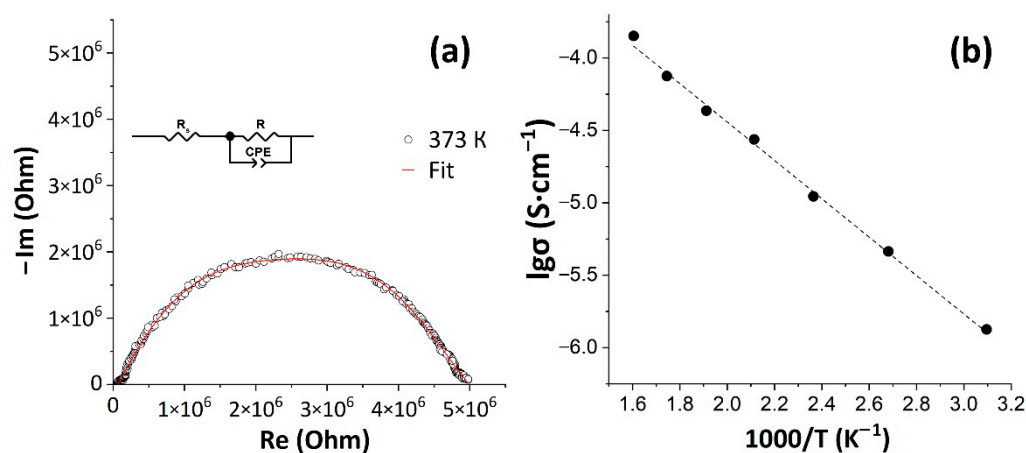


**Figure 7.** The impedance spectrum of a SnO<sub>2</sub> thick film at a measurement temperature of 373 K (a) and temperature dependence of its total electrical conductivity (b) (the black markers indicate experimental values, and the dashed line is the result of linear approximation).

As a result, it has been shown that the electrical conductivity of the coating linearly increased with temperature rising from 50 to 350 °C. Overall increase was by two orders of magnitude—from  $1.23 \cdot 10^{-6}$  to  $1.22 \cdot 10^{-4}$  S·cm<sup>−1</sup> (Figure 7b). That is characteristic of tin dioxide-based semiconductor materials and is caused by ionization of defects (oxygen vacancies) which promotes the increase in concentration and mobility of charge carriers [55].

### 3.5. Chemosensory Properties of SnO<sub>2</sub> Film

The formed SnO<sub>2</sub> thick film was also studied as a receptor component of a resistive gas sensor. At the first stage of the gas sensing study, the sensor responses to various



analytes with concentrations of 100 ppm at different operating temperatures (50–300 °C) were registered in 50 °C increments. A selectivity diagram (Figure 8a) was constructed from the data obtained, demonstrating the dependence of the responses to the various analytes on the operating temperature. As can be seen, the highest response (10.8–63.5) was recorded for C<sub>2</sub>H<sub>5</sub>OH at operating temperatures of 150–250 °C with a maximum at 200 °C. The corresponding columnar selectivity diagram at 200 °C (Figure 8b) shows that the response to 100 ppm C<sub>2</sub>H<sub>5</sub>OH ( $S = 63.5$ ) is significantly higher than that to 100 ppm H<sub>2</sub>, CO, NH<sub>3</sub>, C<sub>6</sub>H<sub>6</sub> and C<sub>3</sub>H<sub>6</sub>O, indicating high selectivity of the studied SnO<sub>2</sub> thick film in ethanol sensing.

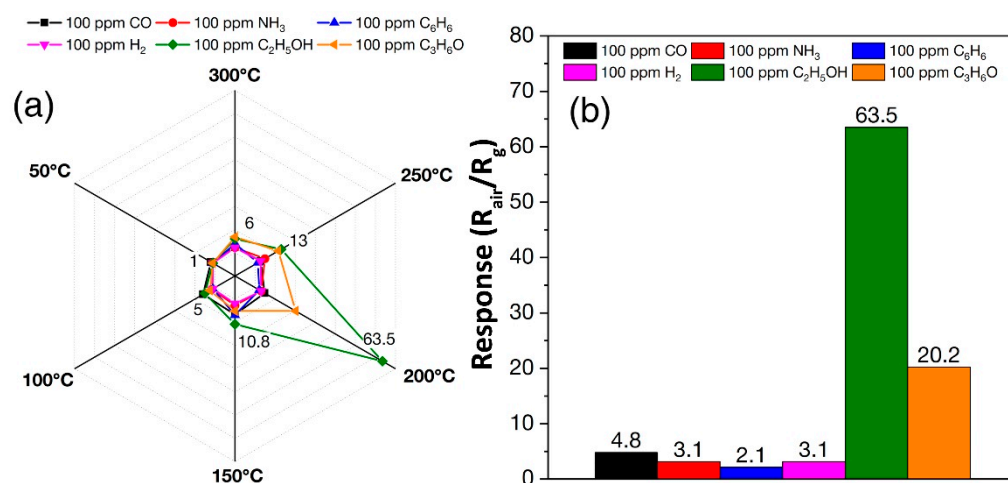


**Figure 8.** Selectivity diagrams showing the sensor responses of the SnO<sub>2</sub> film to various analytes at operating temperatures of 50–300 °C (a) and at 200 °C (b).

Data on the detection of various levels (4–100 ppm) of C<sub>2</sub>H<sub>5</sub>OH demonstrate (Figure 9a,b) that the response increases from 1.4 to 63.5 when the concentration increases from 4 to 100 ppm C<sub>2</sub>H<sub>5</sub>OH. The dependence of the response on concentration can be described by a power function that correlates with the Freundlich isotherm equation, widely used for chemoresistive gas sensors [56,57]:

$$S = kC^a, \quad (2)$$

where  $k$  and  $a$  are the proportionality and exponent constant and represent the adsorption capacity and adsorption intensification, respectively [58]. The parameter  $a$  directly indicates the sensitivity of the material to a particular analyte [56]. In our work,  $a = 1.352$  (Figure 9b), which is a high enough value to quantify the concentration of ethanol in the gas mixture. Such a high ethanol sensitivity is related to the high dispersion state of the oxide nanopowder obtained by the atmospheric pressure solvothermal synthesis, and the high porosity of the SnO<sub>2</sub> film ensured by the microextrusion printing method. It can also be associated with the rapid surface reactions between ethanol and adsorbed oxygen at the specified operating temperature (200 °C).

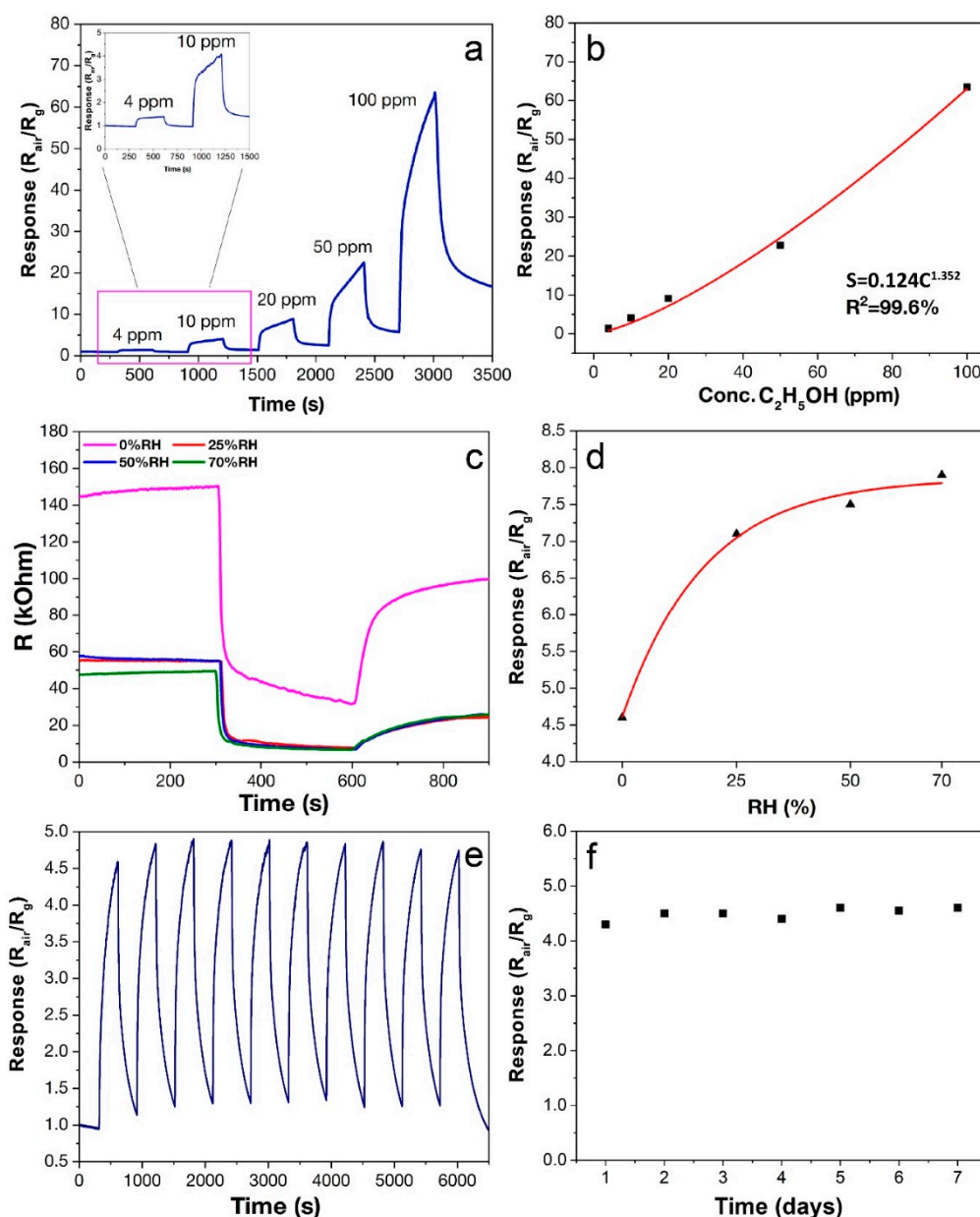
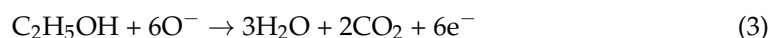


**Figure 9.** Dependence of the sensor response on the concentration (4–100 ppm) of  $C_2H_5OH$  (a,b), change of resistance upon detection of 10 ppm  $C_2H_5OH$  at 0–70% RH (c) and dependence of the response on 10 ppm  $C_2H_5OH$  at different humidity (d), signal reproducibility when detecting 10 ppm  $C_2H_5OH$  (e) and long-term stability of the  $SnO_2$  thick film (f). The operating temperature in all cases was 200 °C.

The mechanism of ethanol detection by the  $SnO_2$  film can be described using the generally accepted model for n-type semiconductors. At elevated temperatures, sorbed oxygen ions ( $O^-$ ,  $O^{2-}$  and  $O_2^-$ ) are formed on the surface of the material through the interaction of sorbed oxygen molecules with electrons from the  $SnO_2$  conduction band [59]. As a result, an electron depletion layer is formed on the semiconductor surface and the interaction with the analyte occurs with the participation of active oxygen ions ( $O^-$  particles prevail at 200 °C [60]).

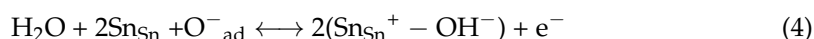
During  $C_2H_5OH$  oxidation, various intermediate products are formed on the surface of  $SnO_2$  [61]: ethoxy groups ( $C_2H_5O^-$ ), acetaldehyde ( $CH_3CHO$ ), ethylene ( $C_2H_4$ ), methane

(CH<sub>4</sub>) and acetic acid (CH<sub>3</sub>COOH). However, the final products of the reaction are carbon dioxide and water [19,62]:

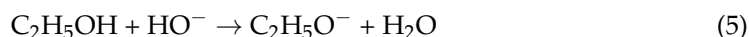


The released electrons enter the conduction band of SnO<sub>2</sub>, resulting in a decrease in electrical resistance (Figure 9c) and the occurrence of a chemoresistive response. Analyzing the obtained signals when detecting ethanol (Figure 9a), it should be noted that their shape is sharp, which indicates a sufficiently long equilibrium establishment time. The ethanol oxidation process (Equation (3)) is a multistep process. As mentioned above, the resulting intermediate products directly affect the equilibrium establishment time, which is reflected both in the shape of the signal obtained and in the overall kinetics of the entire process.

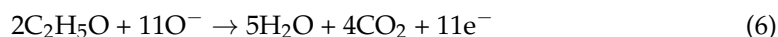
In order to study the effect of humidity on the sensor response, the measurements on the detection of 10 ppm C<sub>2</sub>H<sub>5</sub>OH at 25, 50 and 70% RH were carried out (Figure 9c). As can be seen, in a humid environment there is a significant decrease in resistance both in the baseline (air) and upon ethanol detection. At increased humidity, water molecules react with the SnO<sub>2</sub> surface to form hydroxyl groups [63,64]:



As a result of this reaction, additional electrons are generated, which enter the conduction band of SnO<sub>2</sub>, leading to a decrease in resistance, as was observed in our case. Hydroxyl groups on the SnO<sub>2</sub> surface occupy active sorption centers, thereby reducing the number of sorbed analyte molecules, which leads in many cases to a decrease in the sensor-response value [19,65]. However, in our case, despite the decrease in resistance, the ethanol response value increased at elevated humidity (Figure 9d). Similar behavior has also been previously observed in a number of studies, although it is hardly typical [61,66,67]. There is no single explanation for this phenomenon, but it might be attributed to the formation of ethoxy groups (C<sub>2</sub>H<sub>5</sub>O<sup>−</sup>) on the SnO<sub>2</sub> surface after the ethanol reaction with hydroxyl groups:



The formed ethoxy groups can be further oxidized to CO<sub>2</sub> and H<sub>2</sub>O [61]:



The electrons released as a result of the reaction enter the conduction band of SnO<sub>2</sub>, which leads to a decrease in resistance. The reaction (6) is probably limited in a humid environment, which explains the increased response to ethanol. In the case of ethanol detection in a humid environment, this behavior is primarily associated with the intense surface reactions between ethanol, ion-sorbed oxygen and hydroxyl groups at the specified operating temperature (200 °C). The reproducibility of the sensor signal when detecting 10 ppm C<sub>2</sub>H<sub>5</sub>OH (Figure 9e) and the long-term stability of the obtained thick SnO<sub>2</sub> film (Figure 9f) were also evaluated in the study. As can be seen from the measurement results, the material shows high reproducibility and stability of chemosensor characteristics, which is extremely important for practical reasons.

Table 1 summarizes a literature analysis of ethanol-sensitive oxide materials used as the receptor layer for chemoresistive gas sensors since 2015. Different parameters were considered when evaluating the performance: operating temperature, analyte concentration, response value and relative humidity. As can be seen, the SnO<sub>2</sub> thick film obtained in our study has a relatively low operating temperature for ethanol detection (200 °C), which is important with regard to the energy efficiency of gas sensors. Moreover, the obtained material is characterized by a low gas threshold starting from the concentration of 4 ppm, which is important for prompt impurity detection in the monitored atmosphere. In addition, it should be noted that this paper examined humidity effect (in a wide range) on the chemosensory properties of the obtained tin dioxide film, which is rarely found in

the literature, although this parameter often has a fundamental influence on the functional characteristics of the material [68–70].

**Table 1.** Characteristics of metal oxide chemoresistive gas sensors for ethanol.

Material	Temperature, °C	Concentration, ppm	Response (S)	S Calculation Formula	Relative Humidity, %	Reference
MoO <sub>3</sub>	250	100	19.8	R <sub>air</sub> /R <sub>g</sub>	0	[71]
Al <sub>2</sub> O <sub>3</sub> -ZnO	300	1	53	(ΔR/R <sub>air</sub> ) × 100		[72]
ZnSnO	450	20–500	3.21–31.18	R <sub>air</sub> /R <sub>g</sub>		[73]
NiO	130	100	1.68		12	[74]
α-Fe <sub>2</sub> O <sub>3</sub>	300	100	29.64–37.57		~65	[75]
CuO	300–450	100	2.30–9.10		0	[76]
ZnO	RT/175 °C	2–100	22.9–59.6/90.5–321.7	(ΔR/R <sub>air</sub> ) × 100	~55	[77]
In <sub>2</sub> O <sub>3</sub>	270	0.5–100	1.6–66	R <sub>air</sub> /R <sub>g</sub>	0	[78]
TiO <sub>2</sub>	350–450	50–150	1.8–6.5			[79]
V <sub>2</sub> O <sub>5</sub>	330	50–1000	1.19–9.09			[80]
SnO <sub>2</sub>	190	20–1000	35.6–120		50–70	[81]
SnO <sub>2</sub>	100–300	50	9–31		35 ± 5	[82]
SnO <sub>2</sub>	160–340	20–1000	21–50	(ΔR/R <sub>air</sub> ) × 100	0	[83]
SnO <sub>2</sub>	350	10–30	0.7–1			[84]
SnO <sub>2</sub>	200–400	10–500	21.96–207.68			[85]
SnO <sub>2</sub>	150–300	2000	1.25–1.6			[86]
SnO <sub>2</sub>	230	200	24.9	R <sub>air</sub> /R <sub>g</sub>	30–90	[87]
SnO <sub>2</sub>	200	56–446	62–86	(ΔR/R <sub>air</sub> ) × 100	0	[88]
SnO <sub>2</sub>	260	50–1000	274.5	R <sub>air</sub> /R <sub>g</sub>		[89]
SnO <sub>2</sub>	200–400	19.4–100	1–20			[90]
SnO <sub>2</sub>	150–300	100–500	40–157			[66]
SnO <sub>2</sub>	200	4–100	1.4–63.5		25–70	This work

#### 4. Conclusions

Atmospheric pressure solvothermal synthesis of nanocrystalline SnO<sub>2</sub> (average CSR size— $7.5 \pm 0.6$  nm; particle size— $8.2 \pm 0.7$  nm), which was used as a component of functional inks for microextrusion printing of tin dioxide thick film on the surface of a specialized Pt/Al<sub>2</sub>O<sub>3</sub>/Pt chip, was studied with the use of tin acetylacetonate as a precursor. It was shown that the synthesized tin dioxide, as well as the film formed on its basis, have a cassiterite crystal structure. It was found that the average CSR size of the oxide film is slightly higher ( $8.4 \pm 0.7$  nm) compared to the nanopowder used for its fabrication, which is associated with additional heat treatment of the material. The nanoscale state of the SnO<sub>2</sub> film was confirmed by scanning electron and atomic force microscopy and its local electrophysical properties were evaluated. In particular, the surface capacity and potential distribution maps were built. Using impedance spectroscopy, the temperature dependence of the specific electrical conductivity of the printed SnO<sub>2</sub> film was determined—it was shown that the electrical conductivity increases by two orders of magnitude as the temperature rises from 50 to 350 °C. In addition, it was shown that the printed oxide film is a promising receptor component of resistive gas sensors for low concentrations of ethanol vapor. At the same time, the sensor response increases with humidity, which is not quite typical for such materials. Thus, our study confirmed that the use of tin acetylacetonate as a precursor makes it possible to obtain SnO<sub>2</sub> powder with a developed surface, so



that the resulting thick oxide film demonstrates high chemosensory characteristics in ethanol detection.

**Author Contributions:** Conceptualization, N.P.S.; investigation, N.A.F., I.A.S., P.Y.G., A.S.M., T.L.S., I.A.V., N.P.S.; writing—original draft preparation, N.A.F., I.A.S.; writing—review and editing, N.P.S.; visualization, N.A.F., I.A.S., P.Y.G., A.S.M., T.L.S.; supervision, N.P.S., E.P.S., N.T.K. All authors have read and agreed to the published version of the manuscript.

**Funding:** This work was supported by the Ministry of Science and Higher Education of the Russian Federation (state contract No. 075-03-2022-107, project identifier 0714-2021-0007). SEM and X-ray powder diffraction analysis were performed using shared experimental facilities supported by IGIC RAS state assignment.

**Institutional Review Board Statement:** Not applicable.

**Informed Consent Statement:** Not applicable.

**Data Availability Statement:** Not applicable.

**Conflicts of Interest:** The authors declare no conflict of interest.

## References

- Mai, L.; Zanders, D.; Subaşlı, E.; Ciftiyurek, E.; Hoppe, C.; Rogalla, D.; Gilbert, W.; Arcos, T.D.L.; Schierbaum, K.; Grundmeier, G.; et al. Low-Temperature Plasma-Enhanced Atomic Layer Deposition of Tin (IV) Oxide from a Functionalized Alkyl Precursor: Fabrication and Evaluation of SnO<sub>2</sub>-Based Thin-Film Transistor Devices. *ACS Appl. Mater. Interfaces* **2019**, *11*, 3169–3180. [\[CrossRef\]](#) [\[PubMed\]](#)
- Jang, B.; Kim, T.; Lee, S.; Lee, W.Y.; Kang, H.; Cho, C.S.; Jang, J. High Performance Ultrathin SnO<sub>2</sub> Thin-Film Transistors by Sol-Gel Method. *IEEE Electron Device Lett.* **2018**, *39*, 1179–1182. [\[CrossRef\]](#)
- Liang, D.; Chen, B.J.; Feng, B.; Ikuhara, Y.; Cho, H.J.; Ohta, H. Optimization of Two-Dimensional Channel Thickness in Nanometer-Thick SnO<sub>2</sub>-Based Top-Gated Thin-Film Transistors Using Electric Field Thermopower Modulation: Implications for Flat-Panel Displays. *ACS Appl. Nano Mater.* **2020**, *3*, 12427–12432. [\[CrossRef\]](#)
- Liang, D.D.; Zhang, Y.Q.; Cho, H.J.; Ohta, H. Electric field thermopower modulation analyses of the operation mechanism of transparent amorphous SnO<sub>2</sub> thin-film transistor. *Appl. Phys. Lett.* **2020**, *116*, 143503. [\[CrossRef\]](#)
- Gorobtsov, P.Y.; Fisenko, N.A.; Solovey, V.R.; Simonenko, N.P.; Simonenko, E.P.; Volkov, I.A.; Sevastyanov, V.G.; Kuznetsov, N.T. Microstructure and local electrophysical properties of sol-gel derived (In<sub>2</sub>O<sub>3</sub>-10%SnO<sub>2</sub>)/V<sub>2</sub>O<sub>5</sub> films. *Colloid Interface Sci. Commun.* **2021**, *43*, 100452. [\[CrossRef\]](#)
- Mokrushin, A.S.; Fisenko, N.A.; Gorobtsov, P.Y.; Simonenko, T.L.; Glumov, O.V.; Melnikova, N.A.; Simonenko, N.P.; Bukunov, K.A.; Simonenko, E.P.; Sevastyanov, V.G.; et al. Pen plotter printing of ITO thin film as a highly CO sensitive component of a resistive gas sensor. *Talanta* **2021**, *221*, 121455. [\[CrossRef\]](#) [\[PubMed\]](#)
- Wang, Z.; Zheng, J.; Li, M.; Wu, Q.; Huang, B.; Chen, C.; Wu, J.; Liu, C. Solution-based SnGaO thin-film transistors for Zn- and In-free oxide electronic devices. *Appl. Phys. Lett.* **2018**, *113*, 122101. [\[CrossRef\]](#)
- Zhang, Q.; Ruan, C.; Gong, H.; Xia, G.; Wang, S. Low-temperature and high-performance ZnSnO thin film transistor activated by lightwave irradiation. *Ceram. Int.* **2021**, *47*, 20413–20421. [\[CrossRef\]](#)
- Satoh, K.; Murakami, S.; Kanaoka, Y.; Yamada, Y.; Kakehi, Y.; Sakurai, Y. Effect of postannealing on properties of ZnO-SnO<sub>2</sub> thin film transistors. *J. Vac. Sci. Technol. A* **2018**, *36*, 02C105. [\[CrossRef\]](#)
- Zhu, B.L.; Zhao, X.; Hu, W.C.; Li, T.T.; Wu, J.; Gan, Z.H.; Liu, J.; Zeng, D.W.; Xie, C.S. Structural, electrical, and optical properties of F-doped SnO or SnO<sub>2</sub> films prepared by RF reactive magnetron sputtering at different substrate temperatures and O<sub>2</sub> fluxes. *J. Alloy. Compd.* **2017**, *719*, 429–437. [\[CrossRef\]](#)
- Cong, Y.; Han, D.; Zhou, X.; Huang, L.; Shi, P.; Yu, W.; Zhang, Y.; Zhang, S.; Zhang, X.; Wang, Y. High-Performance Al-Sn-Zn-O Thin-Film Transistor with a Quasi-Double-Channel Structure. *IEEE Electron Device Lett.* **2016**, *37*, 53–56. [\[CrossRef\]](#)
- Yue, J.; Wang, W.; Wang, N.; Yang, X.; Feng, J.; Yang, J.; Qian, Y. Triple-walled SnO<sub>2</sub> at N-doped carbon at SnO<sub>2</sub> nanotubes as an advanced anode material for lithium and sodium storage. *J. Mater. Chem. A* **2015**, *3*, 23194–23200. [\[CrossRef\]](#)
- Heo, J.; Kim, S.B.; Gordon, R.G. Atomic layer deposition of tin oxide with nitric oxide as an oxidant gas. *J. Mater. Chem.* **2012**, *22*, 4599–4602. [\[CrossRef\]](#)
- Zhitomirsky, V.N.; Boxman, R.L.; Goldsmith, S. Plasma distribution and SnO<sub>2</sub> coating deposition using a rectangular filtered vacuum arc plasma source. *Surf. Coat. Technol.* **2004**, *185*, 1–11. [\[CrossRef\]](#)
- Xu, H.Y.; Chen, Z.R.; Liu, C.Y.; Ye, Q.; Yang, X.P.; Wang, J.Q.; Cao, B.Q. Preparation of {200} crystal faced SnO<sub>2</sub> nanorods with extremely high gas sensitivity at lower temperature. *Rare Met.* **2021**, *40*, 2004–2016. [\[CrossRef\]](#)
- He, Y.; Sun, B.; Jiang, L.; Li, X.; Ma, Y.; Wang, K.; Han, P.; Jin, S. Effect of Ag doping on SnO<sub>2</sub> sensing for detecting H<sub>2</sub>S: A first-principles study. *Vacuum* **2021**, *194*, 110587. [\[CrossRef\]](#)

17. Onkar, S.G.; Raghuwanshi, F.C.; Patil, D.R.; Krishnakumar, T. Synthesis, Characterization and Gas Sensing Study of SnO<sub>2</sub> Thick Film Sensor towards H<sub>2</sub>S, NH<sub>3</sub>, LPG and CO<sub>2</sub>. *Mater. Today Proc.* **2020**, *23*, 190–201. [\[CrossRef\]](#)
18. Mahalingappa, K.; Pranesh, G.M.; Manjunath, G.B.; Mundinamani, S.; Molakkalu Padre, S.; Mishra, N.N.; Chandrasekhar, G.S. Low-Temperature Operating Black SnO<sub>2</sub>-Based VOC Sensor Setup. *ACS Omega* **2021**, *6*, 22900–22908. [\[CrossRef\]](#)
19. Ge, W.; Zhang, G.; Wang, P.; Li, Z.; Deng, Y. Highly selective detection of ethanol based on hierarchical three-dimensional SnO<sub>2</sub>: Combining experiment with first-principles calculation. *Sens. Actuators A Phys.* **2021**, *331*, 112994. [\[CrossRef\]](#)
20. Xu, X.; Liu, W.; Wang, S.; Wang, X.; Chen, Y.; Zhang, G.; Ma, S.; Pei, S. Design of high-sensitivity ethanol sensor based on Pr-doped SnO<sub>2</sub> hollow beaded tubular nanostructure. *Vacuum* **2021**, *189*, 110244. [\[CrossRef\]](#)
21. Wu, P.; Li, Y.; Xiao, S.; Chen, J.; Tang, J.; Chen, D.; Zhang, X. SnO<sub>2</sub> nanoparticles based highly sensitive gas sensor for detection of C4F7N: A new eco-friendly gas insulating medium. *J. Hazard. Mater.* **2022**, *422*, 126882. [\[CrossRef\]](#) [\[PubMed\]](#)
22. Li, J.; Yang, M.; Cheng, X.; Zhang, X.; Guo, C.; Xu, Y.; Gao, S.; Major, Z.; Zhao, H.; Huo, L. Fast detection of NO<sub>2</sub> by porous SnO<sub>2</sub> nanotoast sensor at low temperature. *J. Hazard. Mater.* **2021**, *419*, 126414. [\[CrossRef\]](#) [\[PubMed\]](#)
23. Inaba, M.; Oda, T.; Kono, M.; Phansiri, N.; Morita, T.; Nakahara, S.; Nakano, M.; Suehiro, J. Effect of mixing ratio on NO<sub>2</sub> gas sensor response with SnO<sub>2</sub>-decorated carbon nanotube channels fabricated by one-step dielectrophoretic assembly. *Sens. Actuators B Chem.* **2021**, *344*, 130257. [\[CrossRef\]](#)
24. Lu, S.; Zhang, Y.; Liu, J.; Li, H.Y.; Hu, Z.; Luo, X.; Gao, N.; Zhang, B.; Jiang, J.; Zhong, A.; et al. Sensitive H<sub>2</sub> gas sensors based on SnO<sub>2</sub> nanowires. *Sens. Actuators B Chem.* **2021**, *345*, 130334. [\[CrossRef\]](#)
25. Eslamian, M.; Salehi, A.; Nadimi, E. The role of oxygen vacancies on SnO<sub>2</sub> surface in reducing cross-sensitivity between ambient humidity and CO: A first principles investigation. *Surf. Sci.* **2021**, *708*, 121817. [\[CrossRef\]](#)
26. Abokifa, A.A.; Haddad, K.; Raman, B.; Fortner, J.; Biswas, P. Room temperature gas sensing mechanism of SnO<sub>2</sub> towards chloroform: Comparing first principles calculations with sensing experiments. *Appl. Surf. Sci.* **2021**, *554*, 149603. [\[CrossRef\]](#)
27. Suda, A.; Yamamura, K.; Morikawa, A.; Nagai, Y.; Sobukawa, H.; Ukyo, Y.; Shinjo, H. Atmospheric pressure solvothermal synthesis of ceria–zirconia solid solutions and their large oxygen storage capacity. *J. Mater. Sci.* **2008**, *43*, 2258–2262. [\[CrossRef\]](#)
28. Sotelo, J.G.; Bonilla-Ríos, J.; García-Escobar, F.; Gordillo, J.L. Film growth of tetragonal SnO<sub>2</sub> on glass substrate by dip-coating technique for ethanol sensing applications. *Coatings* **2021**, *11*, 303. [\[CrossRef\]](#)
29. Jasim, A.M.; Al-Zubaydi, A.S.J.; Zamel, R.S. Influence of Heat Treatment on the Characteristic of SnO<sub>2</sub> Thin Films for Gas Sensor Application. *J. Phys. Conf. Ser.* **2021**, *1795*, 012034. [\[CrossRef\]](#)
30. Ganchev, M.; Katerski, A.; Stankova, S.; Eensalu, J.S.; Terziyska, P.; Gergova, R.; Popkirov, G.; Vitanov, P. Spin—Coating of SnO<sub>2</sub> thin films. *J. Phys. Conf. Ser.* **2019**, *1186*, 012027. [\[CrossRef\]](#)
31. Gu, F.; Wang, S.F.; Lü, M.K.; Cheng, X.F.; Liu, S.W.; Zhou, G.J.; Xu, D.; Yuan, D.R. Luminescence of SnO<sub>2</sub> thin films prepared by spin-coating method. *J. Cryst. Growth* **2004**, *262*, 182–185. [\[CrossRef\]](#)
32. Ahmad, K.S.; Siraj, H.; Jaffri, S.B.; Alamgir, M.K.; Sohail, M.; Mehmood, R.F.; Rehman, M.U.; Ali, D. Physical Vapor Deposited [Co: Cd(dtc)<sub>2</sub>]/SnO<sub>2</sub> Dual Semiconductor Systems: Synthesis, Characterization and Photo-Electrochemistry. *J. Inorg. Organomet. Polym. Mater.* **2021**, *31*, 2579–2593. [\[CrossRef\]](#)
33. Naeem, R.; Mansoor, M.A.; Munawar, K.; Adnan, A.; Zaharinie, T.; Mohd Zubir, M.N. Versatile Fabrication of Binary Composite SnO<sub>2</sub>-Mn<sub>2</sub>O<sub>3</sub> Thin Films by AACVD for Synergistic Photocatalytic Effect. *J. Electron. Mater.* **2021**, *50*, 3897–3906. [\[CrossRef\]](#)
34. Rieu, M.; Camara, M.; Tournier, G.; Viricelle, J.P.; Pijolat, C.; De Rooij, N.F.; Briand, D. Inkjet printed SnO<sub>2</sub> gas sensor on plastic substrate. *Procedia Eng.* **2015**, *120*, 75–78. [\[CrossRef\]](#)
35. Kassem, O.; Saadaoui, M.; Rieu, M.; Viricelle, J.-P. Synthesis and Inkjet Printing of SnO<sub>2</sub> Ink on a Flexible Substrate for Gas Sensor Application. *Proceedings* **2017**, *3*, 622. [\[CrossRef\]](#)
36. Kassem, O.; Saadaoui, M.; Rieu, M.; Viricelle, J.P. A novel approach to a fully inkjet printed SnO<sub>2</sub>-based gas sensor on a flexible foil. *J. Mater. Chem. C* **2019**, *7*, 12343–12353. [\[CrossRef\]](#)
37. Devabharathi, N.; Umarji, A.M.; Dasgupta, S. Fully Inkjet-Printed Mesoporous SnO<sub>2</sub>-Based Ultrasensitive Gas Sensors for Trace Amount NO<sub>2</sub> Detection. *ACS Appl. Mater. Interfaces* **2020**, *12*, 57207–57217. [\[CrossRef\]](#)
38. Yang, R.; Gao, T.; Li, D.; Chen, Y.; Jin, G.; Liang, H.; Niu, F. Transparent and flexible force sensor based on microextrusion 3D printing. *Micro Nano Lett.* **2018**, *13*, 1460–1464. [\[CrossRef\]](#)
39. Seo, H.; Nishi, T.; Kishimoto, M.; Ding, C.; Iwai, H.; Saito, M.; Yoshida, H. Study of Microextrusion Printing for Enlarging Electrode–Electrolyte Interfacial Area in Anode-Supported SOFCs. *ECS Trans.* **2019**, *91*, 1923–1931. [\[CrossRef\]](#)
40. Seo, H.; Iwai, H.; Kishimoto, M.; Ding, C.; Saito, M.; Yoshida, H. Microextrusion printing for increasing electrode–electrolyte interface in anode-supported solid oxide fuel cells. *J. Power Sources* **2020**, *450*, 227682. [\[CrossRef\]](#)
41. Olate-Moya, F.; Arens, L.; Wilhelm, M.; Mateos-Timoneda, M.A.; Engel, E.; Palza, H. Chondroinductive Alginate-Based Hydrogels Having Graphene Oxide for 3D Printed Scaffold Fabrication. *ACS Appl. Mater. Interfaces* **2020**, *12*, 4343–4357. [\[CrossRef\]](#) [\[PubMed\]](#)
42. Huang, J.; Huang, Z.; Liang, Y.; Yuan, W.; Bian, L.; Duan, L.; Rong, Z.; Xiong, J.; Wang, D.; Xia, J. 3D printed gelatin/hydroxyapatite scaffolds for stem cell chondrogenic differentiation and articular cartilage repair. *Biomater. Sci.* **2021**, *9*, 2620–2630. [\[CrossRef\]](#) [\[PubMed\]](#)
43. Mokrushin, A.S.; Simonenko, T.L.; Simonenko, N.P.; Gorobtsov, P.Y.; Bocharova, V.A.; Kozodaev, M.G.; Markeev, A.M.; Lizunova, A.A.; Volkov, I.A.; Simonenko, E.P.; et al. Microextrusion printing of gas-sensitive planar anisotropic NiO nanostructures and their surface modification in an H<sub>2</sub>S atmosphere. *Appl. Surf. Sci.* **2022**, *578*, 151984. [\[CrossRef\]](#)

44. Simonenko, T.L.; Simonenko, N.P.; Gorobtsov, P.Y.; Klyuev, A.L.; Grafov, O.Y.; Ivanova, T.M.; Simonenko, E.P.; Sevastyanov, V.G.; Kuznetsov, N.T. Hydrothermally synthesized hierarchical  $Ce_{1-x}Sm_xO_{2-\delta}$  oxides for additive manufacturing of planar solid electrolytes. *Ceram. Int.* **2022**, *48*, 22401–22410. [\[CrossRef\]](#)
45. Simonenko, N.P.; Kadyrov, N.S.; Simonenko, T.L.; Simonenko, E.P.; Sevastyanov, V.G.; Kuznetsov, N.T. Preparation of ZnS Nanopowders and Their Use in the Additive Production of Thick-Film Structures. *Russ. J. Inorg. Chem.* **2021**, *66*, 1283–1288. [\[CrossRef\]](#)
46. Simonenko, N.P.; Fisenko, N.A.; Fedorov, F.S.; Simonenko, T.L.; Mokrushin, A.S.; Simonenko, E.P.; Korotcenkov, G.; Sysoev, V.V.; Sevastyanov, V.G.; Kuznetsov, N.T. Printing Technologies as an Emerging Approach in Gas Sensors: Survey of Literature. *Sensors* **2022**, *22*, 3473. [\[CrossRef\]](#)
47. Tong, A.; Pham, Q.L.; Abatemarco, P.; Mathew, A.; Gupta, D.; Iyer, S.; Voronov, R. Review of Low-Cost 3D Bioprinters: State of the Market and Observed Future Trends. *SLAS Technol.* **2021**, *26*, 333–366. [\[CrossRef\]](#) [\[PubMed\]](#)
48. Mokrushin, A.S.; Nagornov, I.A.; Simonenko, T.L.; Simonenko, N.P.; Gorobtsov, P.Y.; Khamova, T.V.; Kopitsa, G.P.; Evzrezov, A.N.; Simonenko, E.P.; Sevastyanov, V.G.; et al. Chemoresistive gas-sensitive ZnO/Pt nanocomposites films applied by microplotter printing with increased sensitivity to benzene and hydrogen. *Mater. Sci. Eng. B Solid-State Mater. Adv. Technol.* **2021**, *271*, 115233. [\[CrossRef\]](#)
49. Mohan Rao, U.; Fofana, I.; Kartheek, R.; Yapi, K.M.L.; Jaya, T. Mineral Oil and Ester Based Oil/Paper Insulation Decaying Assessment by FTIR Measurements. In Proceedings of the 21st International Symposium on High Voltage Engineering, Budapest, Hungary, 26–30 August 2019; pp. 615–624.
50. Wang, Q.; Peng, C.; Du, L.; Li, H.; Zhang, W.; Xie, J.; Qi, H.; Li, Y.; Tian, L.; Huang, Y. Enhanced Performance of Perovskite Solar Cells via Low-Temperature-Processed Mesoporous  $SnO_2$ . *Adv. Mater. Interfaces* **2020**, *7*, 1901866. [\[CrossRef\]](#)
51. Gubbala, S.; Russell, H.B.; Shah, H.; Deb, B.; Jasinski, J.; Rypkema, H.; Sunkara, M.K. Surface properties of  $SnO_2$  nanowires for enhanced performance with dye-sensitized solar cells. *Energy Environ. Sci.* **2009**, *2*, 1302. [\[CrossRef\]](#)
52. Fang, X.; Yan, J.; Hu, L.; Liu, H.; Lee, P.S. Thin  $SnO_2$  Nanowires with Uniform Diameter as Excellent Field Emitters: A Stability of More Than 2400 Minutes. *Adv. Funct. Mater.* **2012**, *22*, 1613–1622. [\[CrossRef\]](#)
53. Babu, B.; Neelakanta Reddy, I.; Yoo, K.; Kim, D.; Shim, J. Bandgap tuning and XPS study of  $SnO_2$  quantum dots. *Mater. Lett.* **2018**, *221*, 211–215. [\[CrossRef\]](#)
54. Tran, V.-H.; Park, H.; Eom, S.H.; Yoon, S.C.; Lee, S.-H. Modified  $SnO_2$  with Alkali Carbonates as Robust Electron-Transport Layers for Inverted Organic Solar Cells. *ACS Omega* **2018**, *3*, 18398–18410. [\[CrossRef\]](#) [\[PubMed\]](#)
55. Yakuphanoglu, F. Electrical conductivity, Seebeck coefficient and optical properties of  $SnO_2$  film deposited on ITO by dip coating. *J. Alloys Compd.* **2009**, *470*, 55–59. [\[CrossRef\]](#)
56. Ambardekar, V.; Bandyopadhyay, P.P.; Majumder, S.B. Understanding on the ethanol sensing mechanism of atmospheric plasma sprayed 25 wt.%  $WO_3$ -75 wt.%  $SnO_2$  coating. *Sens. Actuators B Chem.* **2019**, *290*, 414–425. [\[CrossRef\]](#)
57. McConnell, C.; Kanakaraj, S.N.; Dugre, J.; Malik, R.; Zhang, G.; Haase, M.R.; Hsieh, Y.Y.; Fang, Y.; Mast, D.; Shanov, V. Hydrogen Sensors Based on Flexible Carbon Nanotube-Palladium Composite Sheets Integrated with Ripstop Fabric. *ACS Omega* **2020**, *5*, 487–497. [\[CrossRef\]](#)
58. Sadhanala, H.K.; Nandan, R.; Nanda, K.K. Understanding the ammonia sensing behavior of filter coffee powder derived N-doped carbon nanoparticles using the Freundlich-like isotherm. *J. Mater. Chem. A* **2016**, *4*, 8860–8865. [\[CrossRef\]](#)
59. Ji, H.; Zeng, W.; Li, Y. Gas sensing mechanisms of metal oxide semiconductors: A focus review. *Nanoscale* **2019**, *11*, 22664–22684. [\[CrossRef\]](#)
60. Kim, H.J.; Lee, J.H. Highly sensitive and selective gas sensors using p-type oxide semiconductors: Overview. *Sens. Actuators B Chem.* **2014**, *192*, 607–627. [\[CrossRef\]](#)
61. Gulevich, D.; Rumyantseva, M.; Gerasimov, E.; Khmelevsky, N.; Tsvetkova, E.; Gaskov, A. Synergy effect of Au and  $SiO_2$  modification on  $SnO_2$  sensor properties in vocs detection in humid air. *Nanomaterials* **2020**, *10*, 813. [\[CrossRef\]](#)
62. Motsoeneng, R.G.; Kortidis, I.; Ray, S.S.; Motaung, D.E. Designing  $SnO_2$  Nanostructure-Based Sensors with Tailored Selectivity toward Propanol and Ethanol Vapors. *ACS Omega* **2019**, *4*, 13696–13709. [\[CrossRef\]](#) [\[PubMed\]](#)
63. Zito, C.A.; Perfecto, T.M.; Volanti, D.P. Palladium-Loaded Hierarchical Flower-like Tin Dioxide Structure as Chemosensor Exhibiting High Ethanol Response in Humid Conditions. *Adv. Mater. Interfaces* **2017**, *4*, 1700847. [\[CrossRef\]](#)
64. Großmann, K.; Wicker, S.; Weimar, U.; Barsan, N. Impact of Pt additives on the surface reactions between  $SnO_2$ , water vapour, CO and  $H_2$ ; an operando investigation. *Phys. Chem. Chem. Phys.* **2013**, *15*, 19151–19158. [\[CrossRef\]](#) [\[PubMed\]](#)
65. Liu, Y.; Yao, S.; Yang, Q.; Sun, P.; Gao, Y.; Liang, X.; Liu, F.; Lu, G. Highly sensitive and humidity-independent ethanol sensors based on  $In_2O_3$  nanoflower/ $SnO_2$  nanoparticle composites. *RSC Adv.* **2015**, *5*, 52252–52258. [\[CrossRef\]](#)
66. Zhu, H.; Li, Q.; Ren, Y.; Gao, Q.; Chen, J.; Wang, N.; Deng, J.; Xing, X. A New Insight into Cross-Sensitivity to Humidity of  $SnO_2$  Sensor. *Small* **2018**, *14*, 1703974. [\[CrossRef\]](#)
67. Li, M.; Qiao, L.J.; Chu, W.Y.; Volinsky, A.A. Water pre-adsorption effect on room temperature  $SnO_2$  nanobelt ethanol sensitivity in oxygen-deficient conditions. *Sens. Actuators B Chem.* **2011**, *158*, 340–344. [\[CrossRef\]](#)
68. Yue, J.; Jiang, X.; Yu, A. Adsorption of the OH Group on  $SnO_2$  (110) Oxygen Bridges: A Molecular Dynamics and Density Functional Theory Study. *J. Phys. Chem. C* **2013**, *117*, 9962–9969. [\[CrossRef\]](#)

69. Kaneti, Y.V.; Yue, J.; Moriceau, J.; Chen, C.; Liu, M.; Yuan, Y.; Jiang, X.; Yu, A. Experimental and theoretical studies on noble metal decorated tin oxide flower-like nanorods with high ethanol sensing performance. *Sens. Actuators B Chem.* **2015**, *219*, 83–93. [\[CrossRef\]](#)
70. Song, L.; Dou, K.; Wang, R.; Leng, P.; Luo, L.; Xi, Y.; Kaun, C.-C.; Han, N.; Wang, F.; Chen, Y. Sr-Doped Cubic In<sub>2</sub>O<sub>3</sub>/Rhomboidal In<sub>2</sub>O<sub>3</sub> Homo Junction Nanowires for Highly Sensitive and Selective Breath Ethanol Sensing: Experiment and DFT Simulation Studies. *ACS Appl. Mater. Interfaces* **2020**, *12*, 1270–1279. [\[CrossRef\]](#)
71. Xia, Y.; Wu, C.; Zhao, N.; Zhang, H. Spongy MoO<sub>3</sub> hierarchical nanostructures for excellent performance ethanol sensor. *Mater. Lett.* **2016**, *171*, 117–120. [\[CrossRef\]](#)
72. Goikhman, B.V.; Fedorov, F.S.; Simonenko, N.P.; Simonenko, T.L.; Fisenko, N.A.; Dubinina, T.S.; Ovchinnikov, G.; Lantsberg, A.V.; Lipatov, A.; Simonenko, E.P.; et al. Quantum of selectivity testing: Detection of isomers and close homologs using an AZO based e-nose without a prior training. *J. Mater. Chem. A* **2022**, *10*, 8413–8423. [\[CrossRef\]](#)
73. Jiang, Q.; Wu, C.; Feng, L.; Gong, L.; Ye, Z.; Lu, J. High-response of amorphous ZnSnO sensors for ultraviolet and ethanol detections. *Appl. Surf. Sci.* **2015**, *357*, 1536–1540. [\[CrossRef\]](#)
74. Su, C.; Zhang, L.; Han, Y.; Ren, C.; Chen, X.; Hu, J.; Zeng, M.; Hu, N.; Su, Y.; Zhou, Z.; et al. Controllable synthesis of crescent-shaped porous NiO nanoplates for conductometric ethanol gas sensors. *Sens. Actuators B Chem.* **2019**, *296*, 126642. [\[CrossRef\]](#)
75. Li, X.Q.; Li, D.P.; Xu, J.C.; Han, Y.B.; Jin, H.X.; Hong, B.; Ge, H.L.; Wang, X.Q. Calcination-temperature-dependent gas-sensing properties of mesoporous  $\alpha$ -Fe<sub>2</sub>O<sub>3</sub> nanowires as ethanol sensors. *Solid State Sci.* **2017**, *69*, 38–43. [\[CrossRef\]](#)
76. Umar, A.; Lee, J.-H.; Kumar, R.; Al-Dossary, O.; Ibrahim, A.A.; Baskoutas, S. Development of highly sensitive and selective ethanol sensor based on lance-shaped CuO nanostructures. *Mater. Des.* **2016**, *105*, 16–24. [\[CrossRef\]](#)
77. Beniwal, A.; Sahu, P.K.; Sharma, S. Sol-gel spin coating assisted room temperature operated nanostructured ZnO ethanol sensor with behavior transformation. *J. Sol-Gel Sci. Technol.* **2018**, *88*, 322–333. [\[CrossRef\]](#)
78. Qin, W.; Yuan, Z.; Gao, H.; Meng, F. Ethanol Sensors Based on Porous In<sub>2</sub>O<sub>3</sub> Nanosheet-Assembled Micro-Flowers. *Sensors* **2020**, *20*, 3353. [\[CrossRef\]](#)
79. De Pascali, C.; Signore, M.A.; Taurino, A.; Francioso, L.; Macagnano, A.; Avossa, J.; Siciliano, P.; Capone, S. Investigation of the Gas-Sensing Performance of Electrospun TiO<sub>2</sub> Nanofiber-Based Sensors for Ethanol Sensing. *IEEE Sens. J.* **2018**, *18*, 7365–7374. [\[CrossRef\]](#)
80. Jin, W.; Yan, S.; An, L.; Chen, W.; Yang, S.; Zhao, C.; Dai, Y. Enhancement of ethanol gas sensing response based on ordered V<sub>2</sub>O<sub>5</sub> nanowire microyarns. *Sens. Actuators B Chem.* **2015**, *206*, 284–290. [\[CrossRef\]](#)
81. Zeng, Q.; Cui, Y.; Zhu, L.; Yao, Y. Increasing oxygen vacancies at room temperature in SnO<sub>2</sub> for enhancing ethanol gas sensing. *Mater. Sci. Semicond. Process.* **2020**, *111*, 104962. [\[CrossRef\]](#)
82. He, Y.; Tang, P.; Li, J.; Zhang, J.; Fan, F.; Li, D. Ultrafast response and recovery ethanol sensor based on SnO<sub>2</sub> quantum dots. *Mater. Lett.* **2016**, *165*, 50–54. [\[CrossRef\]](#)
83. Zhang, B.; Fu, W.; Li, H.; Fu, X.; Wang, Y.; Bala, H.; Wang, X.; Sun, G.; Cao, J.; Zhang, Z. Synthesis and characterization of hierarchical porous SnO<sub>2</sub> for enhancing ethanol sensing properties. *Appl. Surf. Sci.* **2016**, *363*, 560–565. [\[CrossRef\]](#)
84. Palla Papavlu, A.; Mattle, T.; Temmel, S.; Lehmann, U.; Hintennach, A.; Grisel, A.; Wokaun, A.; Lippert, T. Highly sensitive SnO<sub>2</sub> sensor via reactive laser-induced transfer. *Sci. Rep.* **2016**, *6*, 25144. [\[CrossRef\]](#)
85. Jiang, X.H.; Ma, S.Y.; Sun, A.M.; Xu, X.L.; Li, W.Q.; Wang, T.T.; Jin, W.X.; Luo, J.; Cheng, L.; Mao, Y.Z. 3D porous flower-like SnO<sub>2</sub> microstructure and its gas sensing properties for ethanol. *Mater. Lett.* **2015**, *159*, 5–8. [\[CrossRef\]](#)
86. Ngoc, T.M.; Van Duy, N.; Hung, C.M.; Hoa, N.D.; Trung, N.N.; Nguyen, H.; Van Hieu, N. Ultralow power consumption gas sensor based on a self-heated nanojunction of SnO<sub>2</sub> nanowires. *RSC Adv.* **2018**, *8*, 36323–36330. [\[CrossRef\]](#) [\[PubMed\]](#)
87. Zhang, L.; Tong, R.; Ge, W.; Guo, R.; Shirsath, S.E.; Zhu, J. Facile one-step hydrothermal synthesis of SnO<sub>2</sub> microspheres with oxygen vacancies for superior ethanol sensor. *J. Alloys Compd.* **2020**, *814*, 152266. [\[CrossRef\]](#)
88. Lu, C.L.; Chang, S.J.; Weng, T.C.; Hsueh, T.J. A Bifacial SnO<sub>2</sub> Thin-Film Ethanol Gas Sensor. *IEEE Electron Device Lett.* **2018**, *39*, 1223–1225. [\[CrossRef\]](#)
89. Qiang, Z.; Ma, S.Y.; Jiao, H.Y.; Wang, T.T.; Jiang, X.H.; Jin, W.X.; Yang, H.M.; Chen, H. Highly sensitive and selective ethanol sensors using porous SnO<sub>2</sub> hollow spheres. *Ceram. Int.* **2016**, *42*, 18983–18990. [\[CrossRef\]](#)
90. Tan, W.; Yu, Q.; Ruan, X.; Huang, X. Design of SnO<sub>2</sub>-based highly sensitive ethanol gas sensor based on quasi molecular-cluster imprinting mechanism. *Sens. Actuators B Chem.* **2015**, *212*, 47–54. [\[CrossRef\]](#)